Far-Ultraviolet Photometric Characteristics of JSC-1A and LMS-1 Lunar Regolith Simulants: Comparative Investigations with Apollo 10084

C. J. Gimar[1,2], U. Raut[2,1,5], M. J. Poston[2,5], A. Stevanovic[3], S. Protopapa[4,2], T. K. Greathouse[5], K. D. Retherford[2,1,5], J. M. Friday[2,5], and J. T. Grimes[2,5]

[1]Department of Physics and Astronomy, University of Texas at San Antonio, San Antonio, TX 78249.

[2]Center for Laboratory Astrophysics and Space Science Experiments (CLASSE), Space Science and Engineering Division, Southwest Research Institute, San Antonio, TX, 78238.

[3]Kleberg Advanced Microscopy Center, University of Texas at San Antonio, San Antonio, TX 78249.

[4] Department of Space Studies, Southwest Research Institute, Boulder, CO 80302, USA.

[5]Space Science and Engineering Division, Southwest Research Institute, San Antonio, TX, 78238.

Corresponding author: Caleb Gimar (caleb.gimar@contractor.swri.org)

Key Points:

- We compare far-UV bidirectional reflectance of JSC-1A, LMS-1, and Apollo 10084 soil to deconvolute space weathering and composition effects
- JSC-1A is brighter in the far-UV and shows a steeper blue spectral slope than LMS-1 and Apollo 10084, consistent with its low Ti content
- JSC-1A and LMS-1 mostly forward scatter in the far-UV, likely from absence of space weathering features in backscattering 10084 grains

Abstract

We have characterized the far-ultraviolet (FUV) spectro-photometric response of lunar soil simulants JSC-1A and LMS-1, reporting notable differences from our previous results for Apollo soil 10084 (Raut et al., 2018). While JSC-1A and LMS-1 were designed to emulate the geotechnical and compositional properties of a low-Ti and high-Ti mare soil respectively, these terrestrial simulants lack "space weathering" attributes such as the nanophase iron present in the weathered rims of Apollo grains and glassy agglutinates. Photometric analyses of the JSC-1A phase curves reveal a ~ 3-4 fold increase in single scattering albedo (SSA) and a forward scattering behavior compared to 10084. LMS-1 is shown to have SSA nearly twice that of 10084 and a near isotropic reflectance. Additionally, both JSC-1A and LMS-1 spectra present a blue slope in the FUV, with the JSC-1A slope ~ 10× larger than that reported for the 10084 soil. Our analyses imply that low-Ti content, corroborated using energy dispersive x-ray spectroscopy, correlates to brighter FUV reflectance and a greater spectral blue slope for JSC-1A, while space weathering components likely contribute to the backscattering of FUV light by the Apollo soil relative to both simulants. Further work with an extended set of Apollo soils is warranted to deconvolute the relative contributions of weathering and composition to their FUV spectro-photometric response.

Plain Language Summary

We compare the far-ultraviolet (115-200 nm) reflectance properties of the lunar mare soil simulants JSC-1A and LMS-1 to that of Apollo soil 10084, a lunar mare soil collected by the Apollo 11 mission at Mare Tranquillitatis. The reflectance spectra of both simulants and the Apollo 10084 sample show a blue slope, meaning they reflect more light at shorter wavelengths. Previous studies have linked this blue slope in lunar soils to space weathering features, although our results point to other compositional differences such as titanium-bearing mineral content influencing this phenomenon. JSC-1A and LMS-1 scatter far-ultraviolet light either away from the direction of incidence (forward scattering) or in all directions (isotropic), while Apollo 10084 scatters light toward the direction of incidence (backscattering). The backscattering observed in Apollo 10084 may be a result of nanophase iron generated in the exterior rims of the soil grains through the reduction of native iron oxide by solar wind and micrometeorites, a space weathering feature not present in the terrestrial simulants.

1 Introduction

In the decades following the retrieval of the Apollo samples, many terrestrially synthesized analogs to these samples have been produced that attempt to best match the bulk mineralogical and geotechnical properties of the lunar soils. However, these analogs generally lack space weathering features inherent to lunar grains (e.g., Pieters & Noble, 2016), and the chemical composition of these analogs (e.g., titanium-bearing mineral content) varies depending on the Apollo soil sample emulated in their formulation. The space weathering features, including nanophase iron ($npFe^0$) and agglutinates, along with other compositional differences, may affect the far-ultraviolet (FUV) reflectance spectra of the lunar soil. The availability of unweathered terrestrial analogs presents an opportunity to test the possible contributions of space weathering and mineralogical/chemical content on FUV reflectance properties and provide context for an improved understanding of the photometric response of Apollo soils.

Previous studies into the relationship between FUV reflectance spectra and space weathering have either focused on observational comparisons of planetary bodies of similar composition yet differing perceived maturity (see Vilas & Hendrix, 2015 for a comparison of asteroids) or more generally compared the FUV reflectance of several lunar soils in a laboratory setting (Wagner et al., 1987). In each instance, the enhancement of reflectance in the FUV compared to visible (~ 400 nm) wavelengths was attributed to the presence of $npFe^0$ resultant of solar wind and micrometeoroid bombardment of iron-bearing minerals in the examined soils. Previous work on Apollo 10084 (Raut et al., 2018) has confirmed the blue slope in the FUV (115-200 nm) reflectance of this mature lunar mare soil, and also observed anisotropic backscattering at these FUV wavelengths, which may be attributable to space weathering features. Furthermore, observations of the lunar surface using the Lunar Reconnaissance Orbiter (LRO) Lyman Alpha Mapping Project (LAMP) data show FUV spectral bluing in both mare and highland regions (Liu et al., 2018) and show that the Lyman-α albedo is greater for more mature regions of the lunar surface as opposed to less mature regions (Byron et al., 2019). LAMP results have also determined the brightness ratio between the Off-band (155-190 nm) and On-band (130-155 nm) albedo to be higher for less mature highlands and vice versa, although this relationship was not observed for the mare regions (Byron et al., 2020).

There is also evidence that FUV spectral bluing is not exclusive to planetary surfaces with $npFe^0$ inclusions; for instance, FUV reflectance spectra of the icy moons Europa (Becker et al., 2018) and Ganymede (Molyneux et al., 2020) show spectral bluing while their surfaces likely contain little to no $npFe^0$. Recent modeling by Penttilä et al. (2020) did not find enhanced reflectance correlated with decreasing wavelength as a result of increased nanophase Fe inclusions; however, their analysis did not extend into the FUV shorter than 200 nm. The relationship between spectral bluing, $npFe^0$, and other surface characteristics becomes more complicated considering results from LAMP, showing the spectral bluing to be more descriptive of decreasing reflectance longward of 160 nm (Hendrix et al., 2016; Byron et al., 2021) rather than increasing reflectance shortward of 160 nm. Other surface compositional differences (e.g., abundance of FeO, plagioclase, and silicates) besides $npFe^0$ correlate to reflectance > 170 nm as well (Byron et al., 2021).

To understand the roles composition and space weathering play in the FUV reflectance of lunar soils and to remedy a general dearth of laboratory FUV reflectance datasets, we have obtained FUV reflectance spectra of unweathered terrestrial analogs JSC-1A and LMS-1 and applied Hapke modeling to quantify their far-ultraviolet photometric response. JSC-1A and LMS-1 are designed to replicate the chemical properties of a low-titanium and high-titanium lunar mare soil respectively, making for a suitable comparison to our previous measurements of the Apollo 10084 retrieved from a mare region of the Moon. This investigation utilizes the same instrumentation—the Southwest Ultraviolet Reflectance Chamber (SwURC)—used in the Raut et al. (2018) for Apollo 10084 measurements. Using these methods in conjunction with energy dispersive X-ray analysis, we find that the low-Ti JSC-1A exhibits a brighter reflectance in the FUV and a more pronounced spectral bluing as compared to the high-Ti Apollo 10084 and LMS-1, suggesting that chemical/mineralogical contents such as titanium-bearing minerals are likely a strong contributor to the FUV spectral bluing. JSC-1A and LMS-1 are forward scattering to isotropic in their reflectance, different from the backscattering Apollo 10084, supporting that the presence of weathering features contribute to the preferential backscattering.

2 Instrumentation and Experimental Procedures

2.1 Instrumentation

The optomechanical layout of the SwURC facility used to obtain the bidirectional reflectance measurements of lunar simulants (JSC-1A, LMS-1) is shown in Figure 1a. Light from a 30-W sealed-tube deuterium lamp (McPherson Model 632) illuminates the entry slit of a McPherson 234-302 vacuum ultraviolet scanning monochromator, following reflection off a focusing mirror. The monochromator houses a MgF_2-coated Al holographic grating (2,400 grooves/mm), which directs the first-order diffracted light toward the exit slit and disperses the broadband light spatially such that different wavelengths λ arrive at different locations on the exit slit plane. The grating rotation selects near-monochromatic far-ultraviolet light (±0.5 nm of the desired λ) through the exit slit while sweeping across the 115- to 200-nm band pass. A pair of concave cylindrical MgF_2-coated Al mirrors collimate and steer the light beam toward the main high-vacuum chamber (typically $\sim 10^{-8}$ Torr) that accommodates a retractable sample tray loaded with lunar simulants. The simulant (~ 25 g), which fills a few mm deep square indentation (51 mm × 51 mm) in the aluminum tray, is illuminated by the now collimated monochromatic light beam at a fixed 45° incidence. The size of the beam incident on the simulants is ~ 10 mm × 10 mm, ensuring the light is incident only on the simulant grains, avoiding stray reflections from the Al tray.

A Photonis Magnum 5901 CsI-coated channeltron is mounted on a rotatable armature which intercepts the light reflected (flux P_r) by the lunar simulants at emission angles θ_r from -25° to +75° with respect to the zenith vector ZV (indicated by the dashed vertical line with an arrow in Figure 1b and c). Reflected far-ultraviolet photons striking the CsI photocathode coating eject electrons, which are amplified via secondary cascades generated in six intertwined spiral channels internal to the channeltron. These cascades are guided towards the anode terminal by a potential gradient (1.8 kV). The amplified analog output signal is fed to counting electronics (discriminator, amplifier, and a frequency counter) to produce a digitized signal in units of counts per second (cps). Channeltron rotation in our setup is restricted to the principal plane, defined as the plane containing the incident beam (flux P_i) and the zenith vector. As such, we report here the bidirectional reflectance of the lunar simulants constrained in the principal plane for each pair of incidence and emission angles relative to the zenith vector or equivalently the phase angle, g, which is the angle between the incidence and emission beam.

A unique feature of the SwURC is the ability to measure absolute bidirectional reflectance, circumventing the need for reflectance standards as adopted by previous studies (e.g., Cloutis et al., 2008; Wagner et al., 1987). The absolute reflectance measurement is made possible by (i) the retractable design of the sample tray and (ii) the extended dynamic range of the

Photonis 5901 channeltron. The incident flux P_i is measured with the channeltron positioned at $\theta_r = +135°$ with the sample tray retracted (Figure 1c).

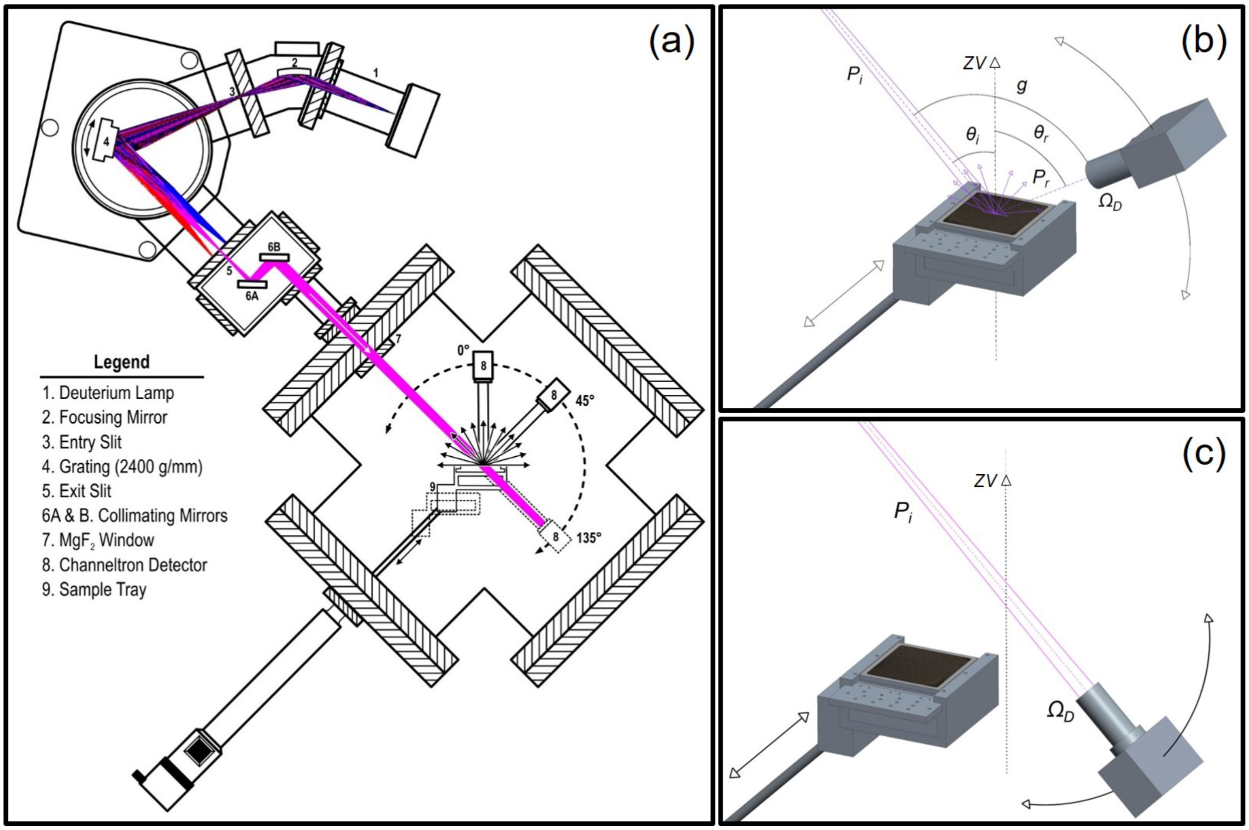

Figure 1. (**a**) Optomechanical layout of the Southwest Ultraviolet Reflectance Chamber. (**b**) The light reflected by the simulants (flux indicated by P_r) is measured at emission angles θ_r spanning -25° to +75° (with respect to the sample tray zenith vector ZV) using the channeltron mounted on a rotating armature. (**c**) The channeltron can also intercept the incident beam (flux P_i) directly when positioned at +135° with the sample tray stowed in the retracted position. The retractable setup of the sample tray along with the extended dynamic range of the channeltron allows for measurement of the absolute bidirectional reflectance of the lunar simulants. Ω_D is the solid angle subtended by the channeltron detector.

2.2 Measurement sequence

Bidirectional reflectance measurement of the lunar simulants is executed in the following sequence:

1. With the sample tray retracted, we measure P_i vs. wavelength λ over 115-200 nm;
2. We measure P_r over -25° to +75° in 1° incremental steps for specific wavelengths: 121.6 (Lyman-α), 125, 130, 135, 140, 150, and 160 nm; and

3. Following diffuse measurements, we retract the sample tray to re-measure P_i and compare it against the initial P_i in Step 1. This step is to verify that the incident flux remains constant to within ± 5% over the measurement duration.

From these measurements, we obtain the bidirectional reflectance distribution function, $f_{BRDF}(\theta_r)$ of the lunar simulants, defined as

$$f_{BRDF}(\theta_r) = \frac{P_r(\theta_r)}{[P_i \cos(-45°)]\Omega_D} \qquad (1)$$

where Ω_D is the solid angle subtended by the channeltron detector. The cos(-45°) term accounts for the reduction in P_i due to non-normal incidence. BRDF has units of sr^{-1}.

2.3 Lunar simulants JSC-1A and LMS-1: source and attributes

We have characterized the far-ultraviolet BRDF of two lunar soil simulants in this study, JSC-1A and LMS-1. Images of the JSC-1A and LMS-1 samples loaded onto the sample tray are shown in Figure 2, alongside the 10084 soil sample on a smaller tray (owing to limited volume).

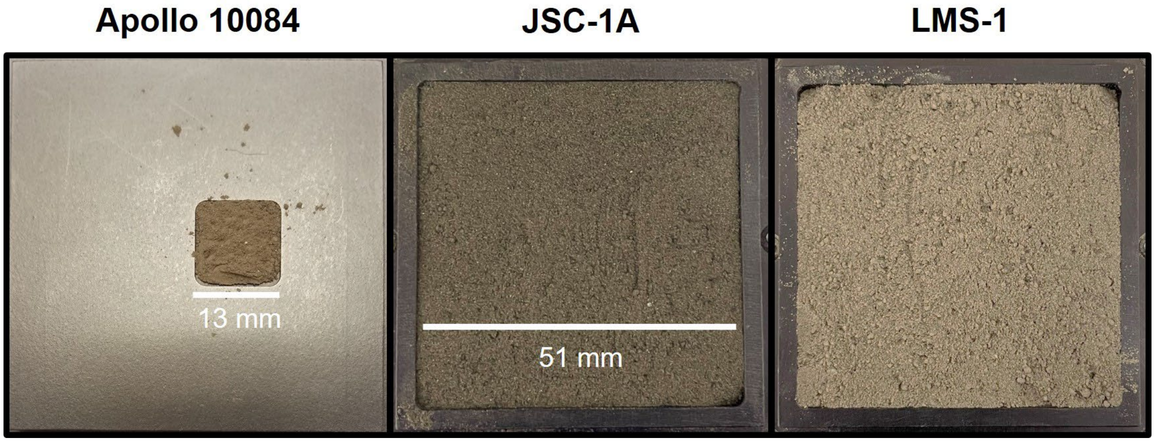

Figure 2. Visual appearance of Apollo soil 10084, JSC-1A, and LMS-1 placed in the anodized aluminum sample trays. A tray with a smaller sample well is used for the smaller quantity of available Apollo soil 10084. Both JSC-1A and LMS-1, available in larger quantities, are placed in large-well trays. Aside from a slight difference in color/tone between the three samples, no other major visual differences are evident.

JSC-1A, developed by Orbital Technology Corporation (McKay et al., 1994), was mined from volcanic ash deposits and produced specifically as an "engineering" simulant designed for terrestrial testing of medium-to-large scale activities such as excavation, materials handling, and construction in support of future human activities on the lunar surface. While the JSC-1 series of simulants replicate the mechanical/geotechnical properties of the average lunar soil fairly well, they also approximate the mineralogy and chemical composition of some lunar soils such as 14163 and 16164. Compared to Apollo 10084 which is enriched in ilmenite ($FeTiO_3$), JSC-1A shows poor Ti-content and lack of space weathering features such as agglutinates and np-Fe^0.

The median JSC-1A grain size is reported as ~ 98-117 µm (Zeng et al., 2010), is nearly twice the 10084 value specifically (McKay et al., 1994; Basu et al., 2000).

LMS-1, developed by Exolith Labs, LLC, is prepared by proportionally mixing rocks and mineral fragments (i.e. polymineralic grains) to approximate the mineralogy of an average mare soil (Britt & Cannon, 2020). LMS-1 maps the chemical make-up of Apollo 10084 with higher fidelity than JSC-1A. Specifically, LMS-1 presents higher Ti-content, and the Ti is more Moon-like, mainly contained in ilmenite. The grain size distribution of LMS-1 closely resembles that of Apollo 10084; the 50 µm LMS-1 median grain size is similar to the 51 µm median size reported for Apollo 10084 (Britt & Cannon, 2020; Basu et al., 2000).

Neither of the simulants include space weathering attributes inherent to Apollo soil 10084 and other lunar soils (McKay et al., 1994; Britt & Cannon, 2020). Specific missing properties include agglutinates, which are mineral aggregates bonded by glassy melts formed by micrometeoroid impacts, and nanophase iron ($npFe^0$) inclusions that occur on grain rims, reduced from native iron oxide by solar wind implantation and micrometeoroid impacts (McKay & Basu, 1983; Papike et al., 1982; Taylor et al., 2001; Keller & McKay, 1997). Additional discussion contrasting the chemical and physical properties of these simulants against Apollo 10084 is presented in Section 4.

2.4 SEM/EDS analysis

To understand the underlying causes for the differences in the BRDF phase curves between the lunar simulants, elemental composition characterization of JSC-1A and LMS-1 was performed using a Hitachi S 5500 cold field-emission scanning electron microscope (SEM). The SEM equipped with a Bruker XFlash 4010 SSD energy-dispersive X-ray detector (EDS) was used to quantify the elemental abundance in the simulants. The grains were deposited onto a carbon tape and inserted via the side-entry sample stage in the gap between upper and lower objective pole pieces. The sample was excited with a 30 keV electron beam and characteristic x-rays were collected by the EDS detector (10 mm^2 collection area) placed ~ 1 cm from the sample at 79^o relative to the sample normal vector. The energy of the x-ray emissions is unique to different elements and the intensity of the emission lines is converted to abundance using the interactive oxide quantification algorithm in the Bruker ESPRIT software, following background subtraction and peak deconvolution. The pixel size of the elemental maps is ~ 0.2 µm.

3 Results

Sample phase curves (BRDF vs. phase angle *g*) for the two simulants at select wavelengths—121.6 nm, 140 nm, and 160 nm—are presented in the top, middle, and bottom panels of Figure 3 respectively. BRDF values are averages of several repeat measurements executed under similar conditions. Phase curves for the simulants (blue circles - JSC-1A; red circles - LMS-1) are compared to those of Apollo 10084 (black circles) obtained in the preceding work (Raut et al., 2018). In general, simulants appear consistently brighter than 10084 mare soil. JSC-1A grains present the highest BRDF values among the three samples, followed by LMS-1, over the measured range of phase angles for the FUV wavelengths investigated. The JSC-1A BRDF values are largest at Lyman-α and are observed to decrease at longer wavelengths. In contrast, the BRDF values of LMS-1 and 10084 grains remain roughly constant versus wavelength (within a factor of ~ 0.3×).

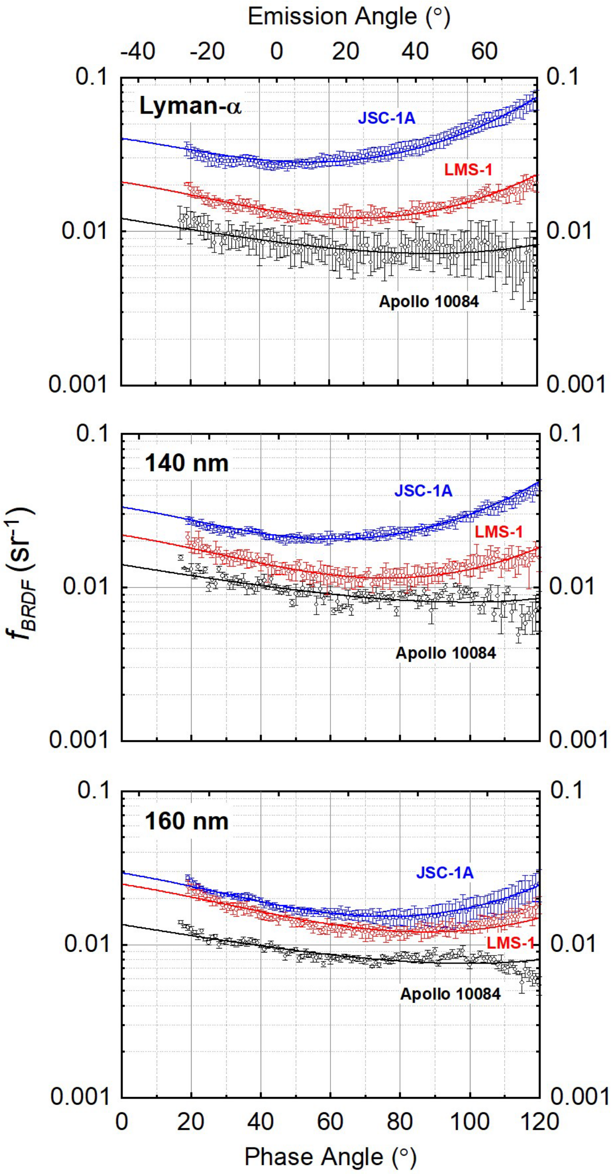

Figure 3. FUV phase curves for JSC-1A, LMS-1, and Apollo soil 10084 at wavelengths λ of 121.6 nm (Lyman-α), 140 nm, and 160 nm. The data points are obtained at 1° increment and fitted to Hapke model (solid curves) to obtain key photometric parameters such as single scattering albedo and scattering phase function. Above 80°, the forward scattering tendency of JSC-1A is evident at Lyman-α, compared to a more isotropic response of LMS-1 and the backward scattering tendency of Apollo soil 10084. At higher wavelengths, JSC-1A converges to the more isotropic curve consistently exhibited by LMS-1, while Apollo soil 10084 remains backward scattering. Also, note the reflectance of JSC-1A decreases with increasing wavelength.

We obtain from Figure 3 a qualitative assessment of the scattering properties of the simulants. For instance, the Lyman-α BRDF of JSC-1A simulant increases steadily with phase angle. The BRDF at larger *g* (~ 120º) is nearly twice the value at smaller phase angles (*g* ~ 20º), suggesting the JSC-1A grains are forward scatterers at least at Lyman-α. The forward scattering behavior appears to decrease with increasing λ, with a nearly isotropic profile emerging at 160 nm. LMS-1, on the other hand, presents a nearly isotropic response at all wavelengths with symmetry at ~ 30° emission angle. Previous work established the backscattering nature of Apollo 10084 (Raut et al., 2018). Quantitative assessment of scattering (isotropic vs. anisotropic) is obtained from the fits of a simplified Hapke model to the phase curves (shown as solid curves in Figure 3) and discussed further in Section 4.

4 Discussion

4.1 Hapke photometric modeling

The bidirectional reflectance distribution function f_{BRDF} according to the Hapke photometric model (Hapke, 2012) and simplified for our experimental conditions is

$$f_{BRDF}(i,e,g) = K\frac{w}{4\pi}\frac{1}{\mu_i+\mu_e}[p(g)+M(i_e,e_e)] \qquad (2)$$

where *K* is the porosity factor, *w* is the volume-averaged single scattering albedo, and μ_i and μ_e are the cosines of the effective angles of incidence and emission, respectively. Altogether, these parameters form the Lommel-Seeliger term, which corrects for pixel scale macroscopic roughness. The $p(g)$ term is the average single-particle scattering phase function, and $M(i_e, e_e)$ approximates the contribution of inter-particle multiple scattering. Our preceding paper (Raut et al., 2018) details the simplifications used to obtain equation (2) from Hapke's comprehensive version that includes treatment of opposition effects, coherent backscattering and shadowing (Hapke, 1981, 1984, 1986, 2008, 2012).

The parameter *K* in Equation 2 is related to the soil porosity *P* as $K(P) = -\ln[1 - 1.209(1 - P)^{2/3}][1.209(1 - P)^{2/3}]^{-1}$ (Hapke, 2008). The average single scattering albedo *w* is the ratio of a particle's scattering efficiency to its extinction efficiency and determines the probability that an incident photon is scattered rather than absorbed. Single scattering albedo is the most robust parameter retrieved from the Hapke photometric model, as shown by the inversion studies of Helfenstein and Shepard (2011).

The average single grain phase function $p(g)$ is approximated with the double-lobed Henyey-Greenstein function:

$$p(g) = \frac{1+c}{2}\frac{1-b^2}{(1-2b\cos(g)+b^2)^{1.5}} + \frac{1-c}{2}\frac{1-b^2}{(1+2b\cos(g)+b^2)^{1.5}} \qquad (3)$$

Here, the lobe size and shape is determined by *b* ($0 \le b \le 1$) and the asymmetry parameter *c* determines the relative strength of the backward and forward lobes (Hapke, 2012), otherwise known as the scattering anisotropy. A symmetric phase function ($c = 0$) implies isotropic scattering, while negative (positive) values of *c* imply forward scattering [FS] (backward scattering [BS]). The intensity and angular distribution of the scattered photons following a single encounter with an average regolith grain is given by the product of $w \times p(g)$. Multiple scattering occurs in a medium composed of grains in mutual contact and is accounted for by the isotropic inter-particle multiple scattering term (Hapke, 1981):

$$M(i,e) = H(i,K,w)H(e,K,w) - 1 \qquad (4)$$

where H is the Ambartsumian-Chandrasekhar function approximated by

$$H(x,K,w) = \left[1 + \frac{2u_x}{K}\right]\left[1 + \frac{2\sqrt{(1-w)}\,u_x}{K}\right]^{-1}$$

Here, x stands in for either angles i or e. For dark, low albedo materials like the Apollo soils and simulants, single scattering from the external surface dominates and multiple scattering contributes minimally to the bidirectional reflectance.

The simplified Hapke equation (Equation 2) contains four free parameters—K, w, b, and c. Since we lack an independent measurement of the soil porosity (or compaction, $1-P$) for our samples, we fit our data with equation (4) while fixing $P = 0.5$ ($K = 1.88$), typical of terrestrial powders (Helfenstein & Shepard, 2011; Johnson et al., 2013). The non-linear Levenberg-Marquardt algorithm (Gill & Murray, 1978) is applied for least-squares fitting of Equation 2 to the laboratory phase curves (Figure 3), allowing us to find optimal values of w, b, and c. Because this method does not necessarily guarantee a global minimum, we use reasonable initial values for these the parameters. Albedo is significantly affected by porosity, since these parameters are coupled in the Hapke model. We find that higher (lower) albedos are required to reproduce the observed BRDFs when higher (lower) porosity is assumed (see Raut et al., 2018 for an extended discussion of porosity effects). We also find that porosity negligibly affects the scattering phase function parameters b and c, obtained from the Hapke fits to the phase curves.

We plot the single-scattering albedo (w) values versus wavelength in Figure 4a. JSC-1A and LMS-1 are both brighter than 10084 soil, although this effect is most pronounced for JSC-1A at shorter wavelengths. Between 130 nm and 160 nm, all samples show a blue slope, where w decreases as wavelength increases; however, the slope is much steeper for JSC-1A than either LMS-1 or Apollo 10084. Compared to the Apollo 10084 slope, the JSC-1A slope is an order of magnitude higher, whereas the LMS-1 blue slope is of the same order of magnitude as Apollo 10084. The higher blue slope of the JSC-1A compared to LMS-1 and 10084 suggests a significant physical and/or chemical attribute common to the latter two and absent in the former to be responsible for the differences in spectral response. Shortward of 130 nm, JSC-1A, and LMS-1 w values decrease slightly at 125 nm before increasing at Lyman-α, suggestive of an absorption dip at ~ 125 nm. Additional w measurements between 120 and 130 nm would be necessary to confirm this absorption feature; previous studies (e.g. Wagner et al., 1987) in soils of similar mineral content do not support an absorption at ~ 125 nm.

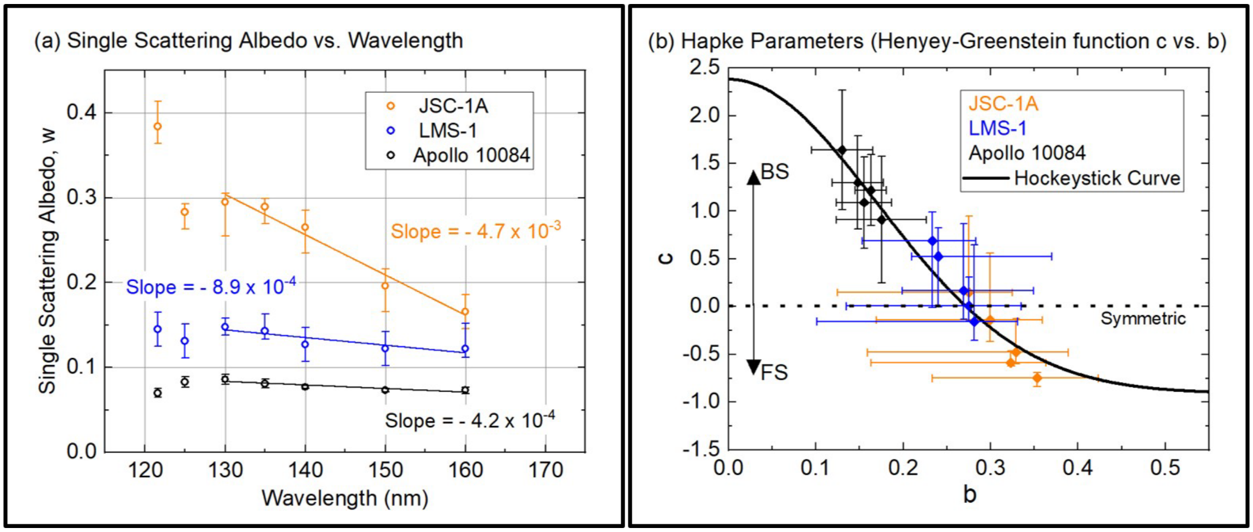

Figure 4. (**a**) Single scattering albedo (*w*) versus wavelength for each tested soil. All three samples show spectral bluing (decreasing brightness as wavelength increases) from 130 nm to 160 nm, however, the slope (nm^{-1}) is an order of magnitude larger for JSC-1A as compared to LMS-1 and Apollo 10084. (**b**) Henyey-Greenstein function anisotropy parameter *c* versus the lobe shape parameter *b* for measurements at five different wavelengths (Table 1). Positive *c* values indicate backward scattering (BS), negative *c* values indicate forward scattering (FS), and zero indicates isotropic scattering (the symmetric black curve). Apollo 10084 is backward scattering, LMS-1 is isotropic to backward scattering, and JSC-1A is forward scattering to isotropic in the far ultraviolet. Within error, the *b-c* data clusters near the “hockey-stick” curve for all soils tested. A soil porosity of 0.5 (K= 1.88) is assumed in the Hapke photometric model used to obtain the plotted parameters from the BRDF phase curve data shown in Figure 3.

In Figure 4b, we plot the asymmetry parameter *c* versus the lobe shape parameter *b*. The wavelengths for each point in Figure 4b are not indicated in the figure for clarity; rather, specific *w*, *b*, and *c* values are given for each soil and incident wavelength in Table 1. The FUV *b-c* values for all three soils follow the empirical “hockey-stick” relation (the black curve). The hockey-stick curve is derived from phase function measurements of an extensive set of 495 particulate samples mostly in the visible to near-infrared (Hapke, 2012; McGuire & Hapke, 1995). The Apollo 10084 *b-c* values for the FUV (black points) all cluster near the upper left side of the plot, where $c > 0$, consistent with anisotropic backscattering properties. Values for LMS-1 (blue points) are more centrally located near the “symmetric” line at $c = 0$, meaning that LMS-1 behaves nearly as an isotropic scatterer, though the data support slight backscattering at longer FUV wavelengths. For JSC-1A, the points mostly collect near the lower plateau of the hockey-stick curve, with $c < 0$ indicative of anisotropic forward scattering. The forward or isotropic FUV photometric anisotropy in both terrestrial analogs contrasts with the backscattering nature of Apollo 10084.

Soil	Parameter	121.6 nm	125 nm	130 nm	135 nm	140 nm	150 nm	160 nm
JSC-1A	w	0.38	0.28	0.30	0.29	0.27	0.20	0.17
	b	0.35	0.33	0.32	0.32	0.33	0.30	0.28
	c	-0.75	-0.66	-0.59	-0.53	-0.48	-0.14	0.15
	RMSE (10^{-3})	0.97	0.71	0.68	0.76	0.74	0.56	0.51
LMS-1	w	0.15	0.13	0.15	0.14	0.13	0.12	0.12
	b	0.28	0.25	0.28	0.26	0.27	0.24	0.23
	c	-0.16	-0.03	0.01	0.10	0.17	0.53	0.69
	RMSE (10^{-3})	0.58	0.71	0.80	0.95	0.66	0.77	0.79
Apollo 10084	w	0.07	0.08	0.09	0.08	0.08	0.07	0.07
	b	0.16	0.19	0.18	020	0.16	0.15	0.13
	c	1.09	0.44	0.91	0.43	1.22	1.30	1.64
	RMSE (10^{-3})	0.60	0.80	1.00	0.80	0.80	0.80	0.55

Table 1. Best fit Hapke parameters derived from phase curve analysis at different wavelengths for JSC-1A, LMS-1, and Apollo 10084. Note: the porosity used is an intermediate value of P=0.5, typical of Earth-based powders and confirmed using our analysis. RMSE is the root-mean-square error between data and modeled curves.

4.2 Linking grain attributes to far-ultraviolet photometric response

Table 2 highlights the major differences in various properties innate to the lunar simulants and 10084 grains (first three rows), along with differences in various spectro-photometric parameters obtained from the Hapke analysis of the phase curves shown in Figure 3 (bottom three rows, italicized). JSC-1A grains, on average, are about twice the size of 10084 or LMS-1 grains. 10084 grains—subjected to micrometeorite impacts and solar wind implantation for eons before being retrieved from the lunar surface—contain glassy agglutinates and nanophase Fe inclusions, especially in the grain rims. These space-weathered attributes are absent in the lunar simulants. In terms of composition/mineralogy, JSC-1A—manufactured to be a geotechnical simulant—differs from 10084 and LMS-1 in composition, mainly with respect to its low Ti abundance and Ti-mineralogy. We discuss next how these innate grain properties are linked to their spectro-photometric response in the far-ultraviolet.

Regolith Property	Apollo 10084	JSC-1A	LMS-1
Composition	High-Ti	Low-Ti	High-Ti
Ti-bearing Mineral Present	Ilmenite	Ti Magnetite*	Ilmenite
npFe^0 & Agglutinates	Yes	No*	No
Grain Size Mean	51 um	~ 90 um	50 um
Anisotropy	*Backward*	*Forward to isotropic*	*Isotropic to backward*
Spectral Blue Slope	*Yes*	*Yes, steep*	*Yes*
Single Scattering Albedo	*~ 0.07-0.08*	*~ 0.17-0.38*	*~ 0.12-0.15*

Table 2. Select innate and spectro-photometric properties of JSC-1A, LMS-1, and Apollo 10084 compared. Note: soil properties previously measured and referenced from earlier studies are in plain text. Photometric parameters derived from Hapke modeling of the BRDF phase curves are italicized. *Sub-micron scale titanium magnetite inclusions in JSC-1A were reported by Taylor et al. (2016) while our own analysis showed little sign of Ti-bearing minerals, a point discussed further in Section 4.2.

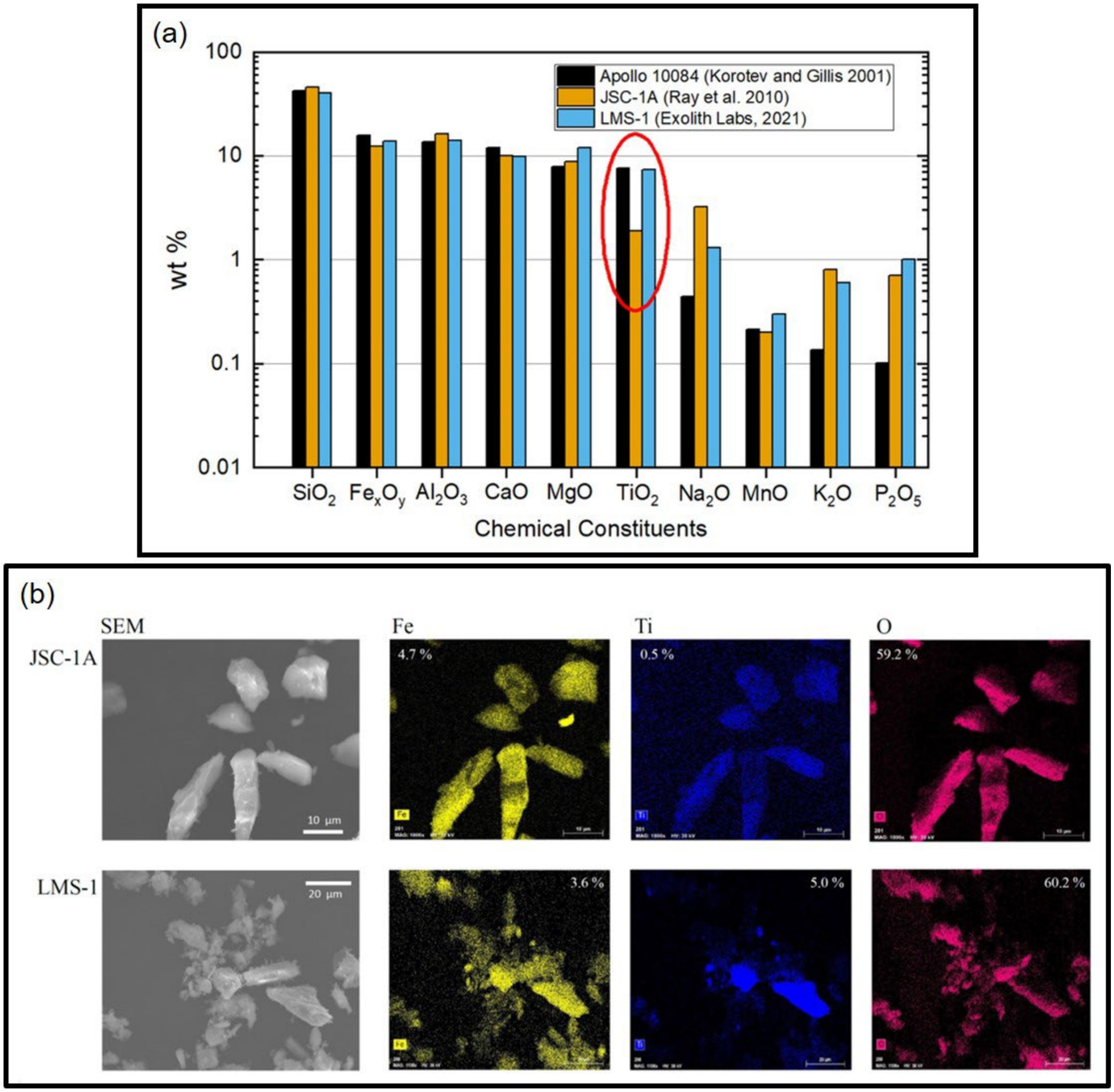

Figure 5. (**a**) Major oxide constituents of Apollo soil 10084, JSC-1A, and LMS-1 compared. Fe_xO_y represents iron oxides generically since oxide states differ between lunar and terrestrial samples. TiO_2 content is circled in red to highlight the commonality between the high-Ti Apollo 10084 and LMS-1 and the disparity compared to low-Ti JSC-1A. Of all chemical constituents > 1 wt%, TiO_2 is not uniform between the soils, due to differences in Ti-bearing mineral content. (**b**) SEM/EDS images of lunar simulants JSC-1A and LMS-1. The simulant grains were excited with a rastered 30 kV electron beam from the SEM source. The Ti abundance in JSC-1A is ~ 10× smaller compared to LMS-1, while Fe and O are nearly identical. Low Ti abundance and absence of ilmenite in JSC-1A may contribute to its brighter albedo compared to 10084 and LMS-1 grains.

LMS-1 and 10084 are reported to be enriched in titanium-bearing minerals (see the TiO_2 amounts in Figure 5a where chemical content is expressed as the presence of major metallic oxides), compared to JSC-1A. Titanium is present mostly as ilmenite (ideal composition - $FeTiO_3$) hosted by the basalts in the Apollo 10084 grains (Kong et al., 2013). Polymineralic grains that contain ilmenite at ~ 4.3 wt % in the LMS-1 formulation closely match 10084 mineralogy (Exolith Labs, 2021). In contrast, JSC-1A reportedly presents different mineralogy with Ti-bearing minerals at a smaller 0.4 wt % abundance (Hill et al., 2007). While other compositional differences exist for minor constituents such as potassium or phosphorous oxides, here we focus on the ~ 4× difference in Ti-content. Our SEM/EDS analysis of the simulant grains corroborates the relative absence of Ti in JSC-1A compared to LMS-1. A 30 kV primary electron beam from a scanning electron microscope produces x-rays, which are further sampled by a Si-based drift detector. Intensities of the characteristic x-ray ($K\alpha_1$ and $K\alpha_2$) emission lines were used to produce the elemental maps shown in Figure 5b. JSC-1A has ~ 10× less elemental Ti compared to LMS-1, while Fe and O abundances are very similar. Abundances of other elements such as Si, Mg, Al, Ca, Na, and K are evaluated via SEM/EDS but not included in Figure 5b. Additionally, the JSC-1A interior revealed by a focused ion beam (Zeiss Crossbeam 340 FIB) milling showed only FeO/MgO dendritic crystal structure within ~ 1 μm from the top surface and scarce Ti-presence throughout the 5-micron cut (see supplemental figure S1). No evidence of Ti-magnetite was observed in our analysis, differing from reports by Taylor et al., 2016.

The correlation between the chemical composition and JSC-1A's bright photometric behavior compared to LMS-1 and 10084 grains, is the poor Ti-bearing mineral content in the JSC-1A grains. Intense Ti^{4+}-O charge transfer absorptions in ilmenite are known to strongly contribute to the low ultraviolet albedo of lunar materials (Tossell, 1979; Cloutis et al., 2008). Ilmenite (Wagner et al., 1987) and pure TiO_2 (Cardona & Harbeke, 1965) absorb strongly in the far-ultraviolet, especially increasing shortward of 150 nm (supplemental figure S2). This may explain why LMS-1 and 10084 grains, enriched in ilmenite/TiO_2, appear darker, while the low-Ti JSC-1A sample presented higher w and larger (by ~ 10× compared to LMS-1) negative spectral slopes. It is difficult to discern if mineralogy (magnetite vs. ilmenite or the dendritic crystals) also affects the absorption and contributes to the brighter JSC-1A compared to low albedo LMS-1 and 10084 grains.

Particle size distribution may affect bidirectional reflectance of granular samples. For example, slightly lower porosity may be possible for the coarser JSC-1A grains (Kiuchi & Nakamura, 2014), which may contribute to the observed higher SSA (Hapke, 2008). However, phase curves from different sizes of sieved JSC-1A grains (< 38 μm versus > 150 μm) did not exhibit a significant difference in brightness compared to the unsieved bulk sample (supplemental figure S3), except at Lyman-α where the finer < 38 μm JSC-1A were 30-40% brighter relative to >150 μm and unsieved counterparts. As such, grain size/porosity variations are unlikely to drive the FUV brightness difference between JSC-1A and 10084/LMS-1, compared to their Ti-compositional difference.

Our finding that lunar simulants, lacking in space-weathered attributes such as glassy agglutinates or nanophase Fe, can also present similar or even higher “blue” slopes compared to the weathered 10084 grains with high maturity index (Morris et al., 1978) does not support the linkage of spectral bluing < 170 nm to space weathering. Several observations of various planetary bodies in the FUV/UV—including the Moon (Lucke et al., 1976) and asteroids (Hendrix & Vilas, 2006, Vilas & Hendrix, 2015, Becker et al., 2020)—show a reversal in the spectral slopes where "red" or positive slopes in the visible and/or near-infrared region reverse into "blue" or negative slopes as they approach the ultraviolet. This slope inversion has previously been attributed to space weathering (Wagner et al., 1987, Vilas and Hendrix, 2015). A recent analysis of LAMP maturity mapping by Byron et al. (2021) explains the FUV bluing behavior as simply a halting of the spectral reddening properties at wavelengths limited to >170 nm. For the <170 nm wavelengths studied here, the spectral slopes are relatively consistent and differences in bulk brightness are more pronounced. While the spectral slope is blue in LAMP datasets for wavelengths <170 nm there is little correlation with space-weathered/mature regions. Our investigations comparing weathered Apollo grains and unweathered simulants show that compositional/mineralogical differences may exert a stronger influence on the magnitude of the albedos in the far-ultraviolet region shortward of 170 nm. Furthermore, recent multi-scale light scattering models that investigate the effects of nanophase Fe inclusions on spectral reflectance (Penttilä et al., 2020) report no evidence of any absolute increase in mid- and near-ultraviolet reflectance (when approaching 200 nm) due to nanophase Fe. Additionally, weathered icy bodies like Europa (Roth et al., 2014; Becker et al., 2018) and Ganymede (Alday et al., 2017; Molyneux et al., 2020) also present a blue slope but are likely without npFe^0 (or other metallic nanophase particles) on their surface, although Becker et al. (2018) did posit micrometeorid implantation in Europa's surface as a source of such metallic particulates. Spectral bluing may also not be unique to the ultraviolet as it has been reported in the visible and near-infrared regions of the spectra of some Saturnian icy satellites and rings (Clark et al., 2008), Utopia Planitia on Mars (Brown et al., 2010) and Comet 17P/Holmes (Yang et al., 2009). The occurrence of blue slopes along the electromagnetic spectrum, based on Rayleigh and Mie scattering theories, was mainly attributed to the interplay of the materials' optical constant and the effective particle size, defined as $\pi D/\lambda$, where D represents the regolith grain diameter (Brown, 2014).

Nanophase inclusions in weathered grain rims may also influence the scattering anisotropy. Of the three sample studies, weathered 10084 appears to effectively backscatter FUV photons, while the compositionally similar but npFe^0-free LMS-1 with similar grain size distribution tends to scatter more isotropically, as evident from the LMS cluster placement (blue filled circles) on the *b*-*c* graph closer to the $c = 0$ symmetric value in Figure 4b. Alternatively, the other effects of space weathering – glassy rims and agglutinates – may be the source of the backscattering, rather than the presence of the opaques. Future investigation with additional mare and highland lunar samples of varying maturity is warranted to fully disentangle the anisotropy dependence on space weathering, grain size, and composition.

We are not able to fully ascertain the possible effects of other sub-micron opaques on the FUV reflectance of JSC-1A. Taylor et al. (2016) reported scanning electron microscopy of JSC-1A, showing small Ti-magnetite inclusions typically several microns in equivalent spherical diameter, although our own SEM analysis did not find Ti-magnetite inclusions in JSC-1A. It is unclear what effect such particles would have on the spectra, but their contribution is likely negligible to FUV reflectance properties since these opaques are probably present throughout the bulk rather than npFe^0 that are preferentially located at the grain rims (~ 100 nm skin, similar to the penetration depth of FUV photons). At the same time, the dendritic FeO/MgO crystals revealed in our SEM imagery are relegated to the outer rims of the JSC-1A grains and cannot presently be ruled out as a contributor to the FUV reflectance properties of JSC-1A. Further investigation will be required to understand the implications of the dendritic crystal structures observed.

5 Conclusions

We measured the diffuse reflectance phase curves of two lunar simulants – JSC-1A and LMS-1 – and compared them with prior similar measurements of Apollo samples 10084 (Raut et al. 2018). The simulants bearing compositional differences in terms of Ti-content and the absence of space weathering attributes provided essential context for an improved understanding of Apollo 10084 photometric response. A Hapke model was used to derive the single scattering albedo (SSA), as well as b and c parameters, for each of the powders. SSA w was found to be lowest for 10084, with LMS-1 just slightly brighter, and JSC-1A significantly brighter. All three powders exhibited blue spectral slope, with LMS-1's slope slightly steeper than 10084, and JSC-1A's slope much steeper. Sample 10084 was found to be backscattering, LMS-1 approximately neutral, and JSC-1A forward scattering, enabling comparisons of their salient properties to help disentangle the driving influences for their FUV reflectance.

Differences among the samples include particle size distribution, the effects of space weathering, titanium abundance, and mineralogy. No strong correlations between particle size distribution and FUV spectral properties were identified in a limited set of sieved sample spectra. Space weathering produced glassy rims, agglutinates, and nanophase iron in Apollo sample 10084, which seems the most likely cause of the backscattering behavior of 10084. Titanium abundance and/or morphology appear to be the most likely factors leading to JSC-1A having a significantly bluer spectral slope and higher SSA than the other two powders. Further work with an extended set of lunar soils with varying composition and maturity is warranted to fully discern the fundamental physical/chemical drivers of FUV photometric response.

Acknowledgements

LRO-LAMP is funded by NASA under contract NNG05EC87C. The development of the SwURC facility was supported by the Southwest Research Institute. Further funding of this work is provided through the NASA Lunar Data Analysis Program grant 80NSSC20K1429. We would like to thank Ashley Reisig for contributing to the instrumentation renders in Figure 1. Thanks also to Jephthah Akene and Andrew Renzetti for their technical assistance with the SwURC facility.

Data Availability Statement

Data associated with this work can be found at https://doi.org/10.5281/zenodo.6929864 (Gimar et al., 2022 [Data set]). All other relevant data is contained in the figures and text of this main publication or in the supplemental materials.

References

Alday, J., Roth, L., Ivchenko, N., Retherford, K. D., Becker, T. M., Molyneux, P., & Saur, J. (2017). New constraints on Ganymede's hydrogen corona: Analysis of Lyman-α emissions observed by HST/STIS between 1998 and 2014. *Planetary and Space Science*, *148*, 35–44. https://doi.org/10.1016/j.pss.2017.10.006

Basu, A., Wentworth, S. J., & McKay, D. S. (2001). Submillimeter grain-size distribution of Apollo 11 soil 10084. *Meteoritics & Planetary Science*, *36*(1), 177. https://doi.org/10.1111/j.1945-5100.2001.tb01818.x

Becker, T. M., Cunningham, N., Molyneux, P., Roth, L., Feaga, L. M., Retherford, K. D., et al. (2020). HST UV Observations of Asteroid (16) Psyche. *The Planetary Science Journal*, *1*(3), 53. https://doi.org/10.3847/PSJ/abb67e

Britt, D. T., & Cannon, K. M. (2020). High Fidelity Lunar Highlands and Mare Regolith Simulants: Enabling Tools for Lunar Surface Exploration and ISRU Development, Presented at the Lunar Surface Science Workshop, held 28-29 May, 2020 (Virtual). LPI Contribution No. 2241, id.5138. https://ui.adsabs.harvard.edu/abs/2020LPICo2241.5138B

Brown, A. J. (2014). Spectral bluing induced by small particles under the Mie and Rayleigh regimes. *Icarus*, *239*, 85–95. https://doi.org/10.1016/j.icarus.2014.05.042

Brown, A. J., Calvin, W. M., McGuire, P. C., & Murchie, S. L. (2010). Compact Reconnaissance Imaging Spectrometer for Mars (CRISM) south polar mapping: First Mars year of observations. *Journal of Geophysical Research: Planets*, *115*(E2). https://doi.org/10.1029/2009JE003333

Byron, B. D., Retherford, K. D., Greathouse, T. K., Mandt, K. E., Hendrix, A. R., Poston, M. J., et al. (2019). Effects of Space Weathering and Porosity on the Far-UV Reflectance of Amundsen Crater. *Journal of Geophysical Research: Planets*, *124*(3), 823–836. https://doi.org/10.1029/2018JE005908

Byron, B. D., Retherford, K. D., Greathouse, T. K., Wyrick, D., Cahill, J. T. S., Hendrix, A. R., et al. (2020). Far-UV Observations of Lunar Rayed Craters with LRO-LAMP. *Journal of Geophysical Research: Planets*, *125*(3), e2019JE006269. https://doi.org/10.1029/2019JE006269

Byron, Benjamin D., Retherford, K. D., Czajka, E., Cahill, J. T. S., Hendrix, A. R., & Greathouse, T. K. (2021). Lunar Surface Composition Constraints from Maturity-corrected Far-ultraviolet Reflectance Maps. *The Planetary Science Journal*, *2*(5), 189. https://doi.org/10.3847/PSJ/ac1d53

Cardona, M., & Harbeke, G. (1965). Optical Properties and Band Structure of Wurtzite-Type Crystals and Rutile. *Physical Review*, *137*(5A), A1467–A1476. https://doi.org/10.1103/PhysRev.137.A1467

Clark, R. N., Curchin, J. M., Jaumann, R., Cruikshank, D. P., Brown, R. H., Hoefen, T. M., et al. (2008). Compositional mapping of Saturn’s satellite Dione with Cassini VIMS and implications of dark material in the Saturn system. *Icarus*, *193*(2), 372–386. https://doi.org/10.1016/j.icarus.2007.08.035

Cloutis, E. A., McCormack, K. A., Bell, J. F., Hendrix, A. R., Bailey, D. T., Craig, M. A., et al. (2008a). Ultraviolet spectral reflectance properties of common planetary minerals. *Icarus*, *197*(1), 321–347. https://doi.org/10.1016/j.icarus.2008.04.018

Cloutis, E. A., McCormack, K. A., Bell, J. F., Hendrix, A. R., Bailey, D. T., Craig, M. A., et al. (2008b). Ultraviolet spectral reflectance properties of common planetary minerals. *Icarus*, *197*(1), 321–347. https://doi.org/10.1016/j.icarus.2008.04.018

Exolith Labs, University of Central Florida. LMS-1 Lunar Mare Simulant. (January 2021). Retrieved August 20, 2021, from https://sciences.ucf.edu/class/simulant_lunarmare/

Gill, P. E., & Murray, W. (1978). Numerically stable methods for quadratic programming. *Mathematical Programming*, *14*(1), 349–372. https://doi.org/10.1007/BF01588976

Gimar, C. J., Raut, U., Poston, M. P., Stevanovic, A., Protopapa, S., Greathouse, T. K., et al. (2022). Far-Ultraviolet Photometric Characteristics of JSC-1A and LMS-1 Lunar Regolith Simulants: Comparative Investigations with Apollo 10084 (Version 1) [Data set]. Zenodo. https://doi.org/10.5281/zenodo.6929864

Hapke, B. (1981). Bidirectional reflectance spectroscopy: 1. Theory. *Journal of Geophysical Research: Solid Earth*, *86*(B4), 3039–3054. https://doi.org/10.1029/JB086iB04p03039

Hapke, B. (1984). Bidirectional reflectance spectroscopy: 3. Correction for macroscopic roughness. *Icarus*, *59*(1), 41–59. https://doi.org/10.1016/0019-1035(84)90054-X

Hapke, B. (1986). Bidirectional reflectance spectroscopy: 4. The extinction coefficient and the opposition effect. *Icarus*, *67*(2), 264–280. https://doi.org/10.1016/0019-1035(86)90108-9

Hapke, B. (2008). Bidirectional reflectance spectroscopy: 6. Effects of porosity. *Icarus*, *195*(2), 918–926. https://doi.org/10.1016/j.icarus.2008.01.003

Hapke, B. (2012). Bidirectional reflectance spectroscopy 7: The single particle phase function hockey stick relation. *Icarus*, *221*(2), 1079–1083. https://doi.org/10.1016/j.icarus.2012.10.022

Helfenstein, P., & Shepard, M. K. (2011). Testing the Hapke photometric model: Improved inversion and the porosity correction. *Icarus*, *215*(1), 83–100. https://doi.org/10.1016/j.icarus.2011.07.002

Hendrix, A. R., & Vilas, F. (2006). The Effects of Space Weathering at UV Wavelengths: S-Class Asteroids. *The Astronomical Journal*, *132*(3), 1396. https://doi.org/10.1086/506426

Hendrix, A. R., Greathouse, T. K., Retherford, K. D., Mandt, K. E., Gladstone, G. R., Kaufmann, D. E., et al. (2016). Lunar swirls: Far-UV characteristics. *Icarus*, *273*, 68–74. https://doi.org/10.1016/j.icarus.2016.01.003

Hill, E., Mellin, M. J., Deane, B., Liu, Y., & Taylor, L. A. (2007). Apollo sample 70051 and high- and low-Ti lunar soil simulants MLS-1A and JSC-1A: Implications for future lunar exploration. *Journal of Geophysical Research: Planets*, *112*(E2). https://doi.org/10.1029/2006JE002767

Johnson, J. R., Shepard, M. K., Grundy, W. M., Paige, D. A., & Foote, E. J. (2013). Spectrogoniometry and modeling of martian and lunar analog samples and Apollo soils. *Icarus*, *223*(1), 383–406. https://doi.org/10.1016/j.icarus.2012.12.004

Keller, L. P., & McKay, D. S. (1997). The nature and origin of rims on lunar soil grains. *Geochimica et Cosmochimica Acta*, *61*(11), 2331–2341. https://doi.org/10.1016/S0016-7037(97)00085-9

Kiuchi, M., & Nakamura, A. M. (2014). Relationship between regolith particle size and porosity on small bodies. *Icarus*, *239*, 291–293. https://doi.org/10.1016/j.icarus.2014.05.029

Kong, W. G., Jolliff, B. L., & Wang, A. (2013). Ti distribution in grain-size fractions of Apollo soils 10084 and 71501. *Icarus*, *226*(1), 891–897. https://doi.org/10.1016/j.icarus.2013.07.007

Korotev, R. L., & Gillis, J. J. (2001). A new look at the Apollo 11 regolith and KREEP. *Journal of Geophysical Research: Planets*, *106*(E6), 12339–12353. https://doi.org/10.1029/2000JE001336

Liu, Y., Retherford, K. D., Greathouse, T. K., Raut, U., Mandt, K. E., Hendrix, A. R., et al. (2018). The Far Ultraviolet Wavelength Dependence of the Lunar Phase Curve as Seen by LRO LAMP. *Journal of Geophysical Research: Planets*, *123*(10), 2550–2563. https://doi.org/10.1029/2018JE005580

Lucke, R. L., Henry, R. C., & Fastie, W. G. (1976). Far-ultraviolet albedo of the moon. *The Astronomical Journal*, *81*, 1162–1169. https://doi.org/10.1086/112000

McGuire, A. F., & Hapke, B. W. (1995). An Experimental Study of Light Scattering by Large, Irregular Particles. *Icarus*, *113*(1), 134–155. https://doi.org/10.1006/icar.1995.1012

McKay, D. S., & Basu, A. (1983). The Production Curve for Agglutinates in Lunar Soils. Presented at Lunar and Planetary Science XIV, March 1983, P. 479-480. https://ui.adsabs.harvard.edu/abs/1983LPI....14..479M

McKay, David S., Carter, J. L., Boles, W. W., Allen, C. C., & Allton, J. H. (1994). JSC-1: A New Lunar Soil Simulant (pp. 857–866). Presented at the Engineering, Construction, and Operations in Space IV, ASCE. Retrieved from https://cedb.asce.org/CEDBsearch/record.jsp?dockey=0086429

Molyneux, P. M., Nichols, J. D., Becker, T. M., Raut, U., & Retherford, K. D. (2020). Ganymede's Far-Ultraviolet Reflectance: Constraining Impurities in the Surface Ice. *Journal of Geophysical Research: Planets*, *125*(9), e2020JE006476. https://doi.org/10.1029/2020JE006476

Morris, R. V. (1978). The surface exposure (maturity) of lunar soils: Some concepts and IS/FeO compilation. *Lunar and Planetary Science Conference Proceedings*, *2*, 2287–2297. https://ui.adsabs.harvard.edu/abs/1978LPSC....9.2287M

Noble, S. K., Pieters, C. M., & Keller, L. P. (2007). An experimental approach to understanding the optical effects of space weathering. *Icarus*, *192*(2), 629–642. https://doi.org/10.1016/j.icarus.2007.07.021

Papike, J. J., Simon, S. B., & Laul, J. C. (1982). The lunar regolith: Chemistry, mineralogy, and petrology. *Reviews of Geophysics*, *20*(4), 761–826. https://doi.org/10.1029/RG020i004p00761

Penttilä, A., Väisänen, T., Markkanen, J., Martikainen, J., Kohout, T., Videen, G., & Muinonen, K. (2020). Rigorous light-scattering simulations of nanophase iron space-weathering effects on reflectance spectra of olivine grains. *Icarus*, *345*, 113727. https://doi.org/10.1016/j.icarus.2020.113727

Pieters, C. M., & Noble, S. K. (2016). Space weathering on airless bodies. *Journal of Geophysical Research: Planets*, *121*(10), 1865–1884. https://doi.org/10.1002/2016JE005128

Raut, U., Karnes, P. L., Retherford, K. D., Davis, M. W., Liu, Y., Gladstone, G. R., et al. (2018). Far-Ultraviolet Photometric Response of Apollo Soil 10084. *Journal of Geophysical Research: Planets*, *123*(5), 1221–1229. https://doi.org/10.1029/2018JE005567

Ray, C. S., Reis, S. T., Sen, S., & O'Dell, J. S. (2010). JSC-1A lunar soil simulant: Characterization, glass formation, and selected glass properties. *Journal of Non-Crystalline Solids*, *356*(44), 2369–2374. https://doi.org/10.1016/j.jnoncrysol.2010.04.049

Roth, L., Saur, J., Retherford, K. D., Strobel, D. F., Feldman, P. D., McGrath, M. A., & Nimmo, F. (2014). Transient Water Vapor at Europa's South Pole. *Science*, *343*(6167), 171–174. https://doi.org/10.1126/science.1247051

Taylor, L. A., Pieters, C. M., Keller, L. P., Morris, R. V., & McKay, D. S. (2001). Lunar Mare Soils: Space weathering and the major effects of surface-correlated nanophase Fe. *Journal of Geophysical Research: Planets*, *106*(E11), 27985–27999. https://doi.org/10.1029/2000JE001402

Taylor, L. A., Pieters, C. M., & Britt, D. (2016). Evaluations of lunar regolith simulants. *Planetary and Space Science*, *126*, 1–7. https://doi.org/10.1016/j.pss.2016.04.005

Tossell, J. A. (1979). Oxygen -> Metal Charge Transfer Energies in Minerals. Presented at the Lunar and Planetary Science X, March 1979, P. 1236–1238. https://ui.adsabs.harvard.edu/abs/1979LPI....10.1236T

Vilas, F., & Hendrix, A. R. (2015). The UV/Blue Effects of Space Weathering Manifested in S-Complex Asteroids. I. Quantifying Change With Asteroid Age. *The Astronomical Journal*, *150*(2), 64. https://doi.org/10.1088/0004-6256/150/2/64

Wagner, J. K., Hapke, B. W., & Wells, E. N. (1987). Atlas of reflectance spectra of terrestrial, lunar, and meteoritic powders and frosts from 92 to 1800 nm. *Icarus*, *69*(1), 14–28. https://doi.org/10.1016/0019-1035(87)90003-0

Yang, B., Jewitt, D., & Bus, S. J. (2009). Comet 17P/Holmes in Outburst: the Near Infrared Spectrum. *The Astronomical Journal*, *137*(5), 4538–4546. https://doi.org/10.1088/0004-6256/137/5/4538

Zeng, X., He, C., Oravec, H., Wilkinson, A., Agui, J., & Asnani, V. (2010). Geotechnical Properties of JSC-1A Lunar Soil Simulant. *Journal of Aerospace Engineering*, *23*(2), 111–116. https://doi.org/10.1061/(ASCE)AS.1943-5525.0000014